Feasibility of Ultrasound Tomography-guided Localized Mild Hyperthermia Using Ring Transducer: *Ex vivo* and *In silico* Studies

Alexander Pattyn[a†], Karl Kratkiewicz[a,b†], Naser Alijabbari[a], Paul L. Carson[c,d], Peter Littrup[e,f], J. Brian Fowlkes[c,d], Nebojsa Duric[e,g], Mohammad Mehrmohammadi[a,h,i*]

[a] Department of Biomedical Engineering, Wayne State University, Detroit, Michigan, 48202, USA

[b] Department of Oncology, Wayne State University, Detroit, Michigan, 48201, USA

[c] Department of Radiology, University of Michigan, Ann Arbor, Michigan, 48109, USA

[d] Department of Biomedical Engineering, University of Michigan, Ann Arbor, Michigan, 48109, USA

[e] Delphinus Medical Technologies, Novi, Michigan, 48374, USA

[f] Ascension Providence Rochester Radiology, Rochester, Michigan, 48307, USA

[g] Department of Imaging Sciences, University of Rochester, Rochester, New York, 14642, USA

[h] Department of Electrical and Computer Engineering, Wayne State University, Detroit, Michigan, 48202, USA

[i] Barbara Ann Karmanos Cancer Institute, Detroit, Michigan, 48201, USA

[†] Equal contribution

[*] Corresponding author:

Email: mehr@wayne.edu,

Tel: +1 (313) 577-1935

Address: 6135 Woodward Ave., Room #3412, Detroit, MI, 48202

Running Title: All-acoustic image-guided mild hyperthermia system

Abstract

Background

As of 2022, breast cancer continues to be the most diagnosed cancer worldwide. This problem persists within the U.S as well, as the American Cancer Society has reported that approximately 12.5% of women will be diagnosed with invasive breast cancer over the course of their lifetime. Therefore, a clinical need continues to exist to address this disease from a treatment and therapeutic perspective. Current treatments for breast cancer and cancers more broadly include surgery, radiation, and chemotherapy. Adjuncts to these methods have been developed to improve the clinical outcomes for patients. One such adjunctive treatment is mild hyperthermia therapy (MHTh), which has been shown to be successful in the treatment of cancers by increasing effectiveness and reduced dosage requirements for radiation and chemotherapies. MHTh-assisted treatments can be performed with invasive thermal devices, non-invasive microwave induction, heating and recirculation of extracted patient blood, or whole-body hyperthermia with hot blankets.

Purpose

One common method for inducing MHTh is by using microwave for heat induction and magnetic resonance imaging (MRI) for temperature monitoring. However, this leads to a complex, expensive, and inaccessible therapy platform. Therefore, in this work we aim to show the feasibility of a novel all-acoustic MHTh system that uses focused ultrasound (US) to induce heating while also using US tomography (UST) to provide temperature estimates. Changes in sound speed (SS) have been shown to be strongly correlated with temperature changes and can therefore be used to indirectly monitor heating throughout the therapy. Additionally, these SS estimates allow for heterogeneous SS-corrected phase delays when heating complex and heterogeneous tissue structures.

Methods

Feasibility to induce localized heat in tissue was investigated *in silico* with a simulated breast model including an embedded tumor using continuous wave US. Here, both heterogenous acoustic and thermal properties were modeled in addition to blood perfusion. We further demonstrate, with

ex vivo tissue phantoms, the feasibility of using ring-based UST to monitor temperature by tracking changes in SS. Two phantoms (lamb tissue, and human abdominal fat) with latex tubes containing varied temperature flowing water were imaged. The measured SS of the water at each temperature were compared against values that are reported in literature.

Results

Results from *ex vivo* tissue studies indicate successful tracking of temperature under various phantom configurations and ranges of water temperature. The results of *in silico* studies show that the proposed system can heat an acoustically and thermally heterogenous breast model to the clinically relevant temperature of 42 $^{\circ}$C while accounting for a reasonable time needed to image the current cross section (200 ms). Further, we have performed an initial *in silico* study demonstrating the feasibility of adjusting the transmit waveform frequency to modify the effective heating height at the focused region. Lastly, we have shown in a simpler 2D breast model that MHTh level temperatures can be maintained by adjusting the transmit pressure intensity of the US ring.

Conclusions

This work has demonstrated the feasibility of using a 256-element ring array transducer for temperature monitoring, however future work will investigate minimizing the difference between measured SS and the values shown in literature. A hypothesis attributes this bias to potential volumetric average artifacts from the ray-based SS inversion algorithm that was used, and that moving to a waveform-based SS inversion algorithm will greatly improve the SS estimates. Additionally, we have shown that an all-acoustic MHTh system is feasible via *in silico* studies. These studies have indicated that the proposed system can heat a tumor within a heterogenous breast model to 42 $^{\circ}$C within a narrow time frame. This holds great promise for increasing the accessibility and reducing the complexity of a future all-acoustic MHTh system.

Keywords— Ultrasound, Tomography, Sound Speed, Mild Hyperthermia, Thermometry, *In silico*, *Ex vivo*, Ring Transducer

INTRODUCTION

The most commonly available methods of cancer treatment are surgery, radiation, and chemotherapy[1]. They are often used in combination to address the local, regional, and systemic extent of cancer, while also attempting to minimize their overall side effect profiles. For most localized tumors, surgical procedures are the standard of care, but minimally invasive treatments are being sought for all stages of cancer. Radiation therapy is a form of localized treatment that is often used to treat the primary tumor, as well as the remaining breast and/or axillary nodes as appropriate to decrease recurrences. However, tumors are often resistant to radiation despite intensive dose regimens that also have considerable associated morbidities, especially for adjacent normal tissues[2]. This radioresistance can in part be attributed to the expressions of MicroRNAs and their control over oncogenic pathways along with the over-expression of insulin-like growth factor-1 receptor (IGF-1R)[3], and human epidermal growth factor receptors (HER)[4]. Chemotherapy is often used to shrink large tumors before surgery in order to reduce complications and to minimize disfigurement. However, limitations of chemotherapy include damage to growing healthy cells due to its systemic nature and drug resistance resulting in changes to the patient treatment plan[5]. There is a clinical need to better target chemotherapy and increase the effectiveness of both radiation and chemotherapy. One method for fulfilling this need is hyperthermia, a method by which a tumor is locally heated to increase its tissue temperature (~42 $^{\circ}$C). Mild hyperthermia therapy (MHTh) has been shown to reduce the dosage requirement of radiation therapy[6] and chemotherapy[7], thereby reducing the damage to healthy surrounding tissues. Chemotherapy can also be targeted more efficiently using MHTh to activate and/or deliver thermosensitive, chemotherapeutic, and immunogenic agents[8,9].

MHTh increases radiation sensitivity through two mechanisms. First by increased tumor perfusion under mild hyperthermic conditions, tissue oxygenation is improved which results in increased tissue radiosensitivity[10]. Secondly, it has been shown that MHTh inhibits cellular DNA-repair proteins involved in the restoration of radiation-induced DNA damage. This in turn potentiates radiation

effects[11]. MHTh has been clinically studied in many different types of cancers including: breast[12,13], bladder[14,15], soft tissue sarcoma[16,17], rectal[18,19], pancreatic[20,21], cervical[22,23], and others[24-27].

Along with improving outcomes by combining MHTh with radiation or chemo hormonal therapies, MHTh can be used to develop a molecular targeted approach. Temperature sensitive liposomes filled with chemotherapeutic agents (e.g. doxorubicin, alvespimycin), are beginning to be studied[9,28]. Rather than systemically injecting, i.e., intravenous (IV), free chemotherapeutic agents - which will affect cells throughout the body - encapsulating the drug in heat sensitive liposomes allows for controlled release only at the heated region. Local tumor tissue concentrations of doxorubicin and alvespimycin were increased 3 to 25 times, compared to IV delivered free drug without tumor heating[9,29-31]. Improved treatment outcomes for current options and the feasibility of their application to new treatment combinations demonstrate the need for advancing MHTh.

MHTh-assisted treatments can be performed with a range of invasive thermal induction devices, non-invasive microwave treatment, heating and recirculation of extracted patient blood, or whole-body hyperthermia with hot blankets. Microwave heat induction is used as the preferred choice of MHTh for deep lying tumors and when combined with other cancer treatments it has shown improved clinical outcomes[32,33]. However, maintaining elevated tissue temperatures relies on real-time temperature monitoring as tissue thermal properties change with increasing temperature. Noninvasive thermometry has been favored over invasive thermocouple placements which usually involves temperature sensitive sequences available with magnetic resonance imaging (MRI)[34]. MRI is capable of measuring both temperature change – through proton resonance frequency (PRF) shifts, and the absolute temperature – via spectroscopic methods or with contrast agents[34]. However, choosing MRI as a temperature sensing and guidance method adds to the complexity and cost of the hyperthermia delivery system as well as reduces the accessibility of the therapy. Additionally, MRI has greater difficulty in measuring the temperature change in fatty tissues using PRF, however alternatives like T_1- and T_2-based approaches are under investigation. These methods currently

encounter issues such as thermal measurements having a non-linear relation at higher temperatures and low temperature sensitivity for T_1 and being time consuming for T_2[34]. These factors contribute to a cumbersome treatment process, thus increasing cost while decreasing patient access to convenient reproducible therapy.

Ultrasound (US) is showing promise to combine these components as it has greatly shown both its utility to generate levels of MHTh in tissue through continuous wave US (CWUS)[35-38] and to measure tissue temperature, derived from tissue sound speed (SS) using US tomography (UST)[39,40]. In UST, reflected acoustical "echoes" can be used to form reflection mode images, whereas transmitted acoustic waves can be used to extract tissue acoustical properties such as SS and attenuation. SS images are often created by extracting the time-of-flights (TOF) between emitter-receiver pairs within UST data, and using those in conjunction with either ray-based or waveform inversion methods[41]. These SS images can then be converted to temperature maps as the relation between SS and temperature is ~2 m/(s°C) between the ranges of 25-42 °C, depending upon tissue type[42,43]. Two factors to consider in a UST/MHTh system are the frequencies and power necessary to perform the imaging and heating procedures. Depending on the US application and tissue of interest; a myriad of frequency probes may be used. However, this will change the field of view and resolution of the reconstructed image. When looking at full breast imaging, we can compare with the SoftVue® imaging system (Delphinus Medical Technologies, Michigan, USA), which performs diagnostic imaging with frequencies in the range of 1-3 MHz[44]. Diagnostic imaging commonly operates in a pressure range of 0.1-1 MPa[45,46]. In an all-US MHTh system, modifying the frequency of the continuous wave (long toneburst) acoustic emissions used for heating will adjust the effective heating radius, so the frequency used will be patient specific. Pressures used for heating also vary depending on application (mild hyperthermia versus HIFU/cavitation). One study has shown that 1.6 MPa peak focal pressure can give 5 °C temperature increase in glycerol[47], however higher focal pressures have been used (4 MPa)[36]. Ring-based UST is currently being used in clinical settings for breast cancer screening, proving the utility of this modality for theranostic purposes[48]. Therefore,

using a ring-UST system has great potential as a combined theranostic device, as it can both induce heat through focused US and monitor temperatures in tissues such as breast, unlike MRI monitoring which requires an external heating modality that must also be MRI compatible (i.e., non-ferromagnetic) and still struggles for thermal accuracy in the predominant component of most women's breast tissue.

In this work, we aim to demonstrate through simulations the potential for using an US ring array system as a means to locally induce heat and maintain elevated temperature in an anatomically accurate numerical breast phantom with an embedded tumor. US and UST have been used previously for combined heating and imaging systems, however these systems typically require the use of two separate transducers[49-52], one for imaging and another for focused ultrasound therapy. When compared to other ultrasound guided focused ultrasound (USgFUS) systems, the system proposed in this manuscript has the advantage of providing more quantitative information than B-mode images alone – such as SS reconstruction. Looking at UST guided focused ultrasound (USTgFUS) systems, such as the system proposed by Azhari[52], current implementations also require separate imaging and heating transducers. These separate modules come in the form of two opposing transducers for tomographic data acquisition and a separate HIFU transducer for heat induction. Traditionally, the weak point for UST thermometry is the extended period of time required to receive enough data for SS inversion. However, due to the ring-array design proposed in this manuscript, the time required for a tomographic scan of a single slice is only 100 ms[53] versus the 10-30 s[52] for the small field-of-view 2D scan from Azhari's system. This allows us to take advantage of the rich information provided by UST while also maintaining a relatively high temporal resolution. Additionally, we build upon our previous work[54]. Given that our current ring-based UST system is designed and developed for imaging applications, experimental heat induction cannot be evaluated due to hardware limitations preventing programmable transmit waveforms. As a result, we have comprehensively investigated heat induction using *in silico* studies. However, we have fully considered the practical settings including geometries identical to the existing ring system and

feasibly implemented waveforms for heat inductions. To summarize, we have performed multiple US induced thermal diffusion simulations for validating the feasibility of an all-US theranostic system. The US forward model outputs a steady state pressure field which was converted to a heat deposition map and used for thermal diffusion modeling of tissue heating. The thermal modeling accounted for system on-time (heating) and off-time (imaging) to show that tissue could still reach MHTh levels without continuous heating. We also ran another 2D US/thermal forward model that showed the ability to adapt US output pressure to maintain elevated MHTh temperatures over a longer duration. Further, we simulated a 3D US forward model of a UST ring-array of finite height at varying central frequencies to show that the effective heating region-of-interest (ROI) height can be adapted for different sized tumors. This would be useful in generating complex, patient-specific sequencing for tumor heating. Finally, we experimentally demonstrate the ability to use UST for monitoring variations in water SS produced from changes in temperature in *ex vivo* phantoms (soft-tissue sarcoma and breast mimic). This showed that the imaging sequences between continuous wave heating periods would be able to monitor changes in tissue temperature in real-time. This feasibility study represents a step toward a practical, fully US-based MHTh treatment system.

Materials and Methods

All-acoustic UST-guided localized mild hyperthermia system

Experimentally, a ring-based UST system was used. This system is comprised of a 256-element ring, 200 mm diameter US transducer (Sound Technology Inc., State College, PA) where the center frequency is 1.5 MHz and the bandwidth is 60%. The ring array has a 2.45 mm element pitch and a 9 mm element height. The sampling frequency of the system is 8.33 MHz due to hardware limitation and the low-frequency operation of the ring UST system. Currently, a custom-built US data acquisition system is used for controlling and powering the ring-array[53]. A polyethylene teraphthalate glycol-modified holder (Stellar Plastics, Detroit, MI) housed the US transducer, the phantom, and coupling medium (distilled and degassed water). The resolution of the SS images

obtained by the system was 4 mm[53]. Other UST systems (even those with no direct application in MHTh) have the following SS resolutions: (1) QT Ultrasound – 1.49mm[55], and (2) Karlsruhe – 0.24mm[56]. While SS measurement resolution is currently limited, we believe that using a more advance waveform inversion algorithm will bring the SS resolution of our system into line with its contemporaries. A schematic of the US ring array system is seen in **Figure 1** showing both imaging and a potential future hyperthermia induction sequence performed by the ring-based system. An SS image of the imaged object is produced through an SS ray-based inversion algorithm alongside a reflection mode US image through traditional back-projection[57,58]. For SS reconstruction, a bent-ray TOF inversion scheme was utilized. Matrix inversion of the experimental data was performed following the methods described in Li et al[59]. This matrix inversion is a non-linear problem due to ray-bending, therefore the Paige and Saunders' LSQR method was used with an initial homogeneous SS starting model[60]. Upon each iteration, the SS model is updated such that the traced rays of the acoustic forward model, and resultant TOFs, converge upon the TOFs of the experimental data. Forward model rays were traced using Klimes' grid travel-time tracing technique[61]. An ultimate therapy sequence plan for the proposed system would be to acquire an initial SS and reflection mode image to localize ROIs and determine waveform delays to focus pressure at the tumor site. This would be followed by sequential on/off periods of heat induction through CWUS and interleaved with SS imaging for real-time temperature monitoring.

Ultrasound thermometry using a ring ultrasound system: ex vivo studies

Using the above system, two phantoms were imaged, both of which contained two latex tubes (Medline DYND50423, USA) of 15 mm diameter carrying temperature-controlled water and used a coupling medium of water. The phantoms were either made from (1) lamb tissue with embedded 20 mm diameter turkey bone, or (2) human abdominal fat – obtained under a protocol approved by Wayne State University Institutional Review Board (IRB). Tissue phantom (1) represents imaging soft tissue sarcoma in human limb, while phantom (2) represents a scenario close to breast cancer. The temperature of the flowing water was controlled using a pump (Bayite BYT-7A108), a temperature

controller (Ink-bird ITC-308S, Shenzhen, China), and a metal heating element (Diximus DX-1000). A schematic of this full system, and images of the two phantoms can be seen in **Figure 2**. All phantoms were imaged with the flowing water being maintained between the ranges of 25-45 $^{\circ}$C. In the case of phantom (1) the tube distances from the bone were 1 and 4 cm.

After performing the imaging sequence for each phantom at each temperature, the SS and reflection images were evaluated with ImageJ [62] image processing toolbox. ROIs and tube locations were identified structurally using the reflection mode image. Using the SS images, average pixel values and standard deviations of the pixels for each tube ROI were taken. An ROI within the background water of the lamb tissue phantom was quantified to show that the SS of the background was unchanging throughout the entirety of the experiment. Literature values of water SS at the experimentally controlled temperatures were compared against the SS reconstructed image values[42].

In silico feasibility studies of localized mild hyperthermia induction using a ring transducer

We evaluated the feasibility of inducing MHTh *in silico* by modeling a ring-shaped US transducer with characteristics mimicking our experimental ring-array UST system. The phantom used as a target was a numerical breast model with an embedded tumor. Three scenarios were considered: (1) 2D acoustic-thermal simulation using emitters – such that the width was modeled, where localized heating was focused at the center of the tumor, (2) 2D acoustic-thermal simulation using emitters, such that the width was modeled, where localized heating was done sequentially at 8 equidistant foci in a ring at half radius of the tumor, and lastly (3) 3D acoustic-thermal simulation using rectangular emitters, where localized heating was focused at the center of the tumor – to compare the effect of Z-directional beamforming with the results from simulation (1). The ring array UST transducer was modeled based on our experimental system where the ring has a 200 mm diameter, composed of 256 elements, where in the 3D acoustic/thermal simulation the elements were modeled as rectangles with a height of 12 mm and a width of ~1.6 mm. The 2D acoustic/thermal

simulations only considered the width.

In all scenarios the k-wave toolbox [63] (MATLAB®, Mathworks, Natick, Massachusetts, USA) was used for both thermal and acoustic forward modeling. The computational grid was based on a pixel/voxel size of 10 points-per-wavelength, see equation 1:

$$dx = \frac{\lambda}{ppw} = \frac{c}{ppw\,f} \qquad (1)$$

where dx is the spatial discretization, λ is the wavelength, ppw is the points-per-wavelength, c is the SS, and *f* is the frequency. The type of computational grid that was used for both the acoustic and thermal simulations was a simple rectangular grid whose spatial discretization was isotropic. For all simulations a CWUS - long tone burst (1.8 s) - signal was used to induce localized heating, the frequency of this signal was 500 kHz with an amplitude of 50 kPa for 2D simulations and 100 kPa for 3D. This resulted in a phantom whose 3D dimensions were 22 cm × 22 cm × 3.6 cm with a spatial discretization of ~ 325 μm. The 2D simulations only used the center z-slice of this phantom, while the 3D simulation used the whole model. The phantom originated from the Optical and Acoustic Breast Phantom Database (OA-breast)[64], and was composed of skin, fibroglandular, fat, blood vessels and surrounding water components. The numerical breast phantom was adapted for our experiment, such that the blood vessels were removed, and a 2 cm diameter spherical tumor was embedded into the center of the breast. The acoustic properties for this phantom are listed in Table 1[65-68].

To determine the SS corrected phase delays for the CWUS, an *in silico* acoustic forward model was used to emit a Dirac delta pulse from the center of the simulated tumor and recorded by the center voxel of each sensor. Under a clinical scenario a SS image would have to be taken before therapy begins and then used to generate the SS-corrected phase delays with the same method as *in silico*. The time-of-arrivals were used to temporally shift all waveforms within each corresponding sensor. In the multi-focus simulation scenario, each of the 8 foci required a forward model run to generate 8 lists of appropriate CWUS delays. These CWUS signals were then emitted in an acoustic forward

model until steady state was achieved. The pressure field was sampled at every pixel/voxel at 17 MHz for the last 2 cycles of steady state. Again, the multi-focus simulation required running 8 separate forward models for each focus within the tumor. The pressure amplitude for all pixels/voxels in the medium was extracted from the recorded time series and a heat deposition map was generated using equation 2:

$$Q = \frac{\mu P^2}{\rho c}$$

(2)

where Q is the heat energy, P is the pressure field, μ is the absorption coefficient, ρ is the density, and c is the SS. We then define a similar medium to model the thermal diffusion. This model solves the Pennes' bioheat equation in 1D, 2D, and 3D, which also accounts for heat loss due to tissue perfusion and heat deposition due to ultrasound absorption[63]. A similar numerical breast phantom as the ultrasound forward model was embedded in the new grid and thermal parameters; thermal conductivity, specific heat, and perfusion were applied (Table 2[65,66,69]). To model perfusion, a blood density of 1060 kg/m^3, blood specific heat of 3617 J/(kg K), and the initial temperature map for the thermal model was set so the breast tissue had a temperature of 37 $^{\circ}$C while the surrounding water was 25 $^{\circ}$C[65].

Heating was performed with on and off periods to represent the time spent performing temperature monitoring mid-therapy with SS imaging (**Figure 3**). Each heating cycle included 1.8 s of on time defined as the heat map generated from the CWUS acoustic forward models described above equation 2 and 0.2 s of off time (imaging time) defined as a period of no heating – heat deposition is zero. The multi-focus simulation used one of the 8 foci heat maps generated in each 1.8 s heating period and cycled through them iteratively. A 0.2 s time interval was set as off-time duration since our expected time required for SS imaging is ~100 ms. The thermal forward model was run in this way for 120 s (60 cycles) for the single focus simulations and 210 s (105 cycles) for the multi-focus simulation with time steps of 20 ms. The rationale for the increase in total therapy time for the multi-focus simulation is due to the additional time needed to reach a final temperature of

~42 °C.

As we investigate how to better dispense acoustic energy within the volume contained by the ring, we began to consider how the steady state acoustic pressure field varies with different frequencies in the Z direction. Again, the k-wave MATLAB toolbox was used for all 3D acoustic simulations. A volume of 24 cm × 24 cm × 2.4 cm was simulated with a grid density variable based on equation 1. The experimental ring array was simulated like the description above with a 200 mm diameter and 256 elements; however, each element was represented by a 12 mm tall line source. The medium was comprised of a water bath containing the acoustic properties seen in Table 1. CWUS waveforms were emitted in phase to focus at the center of the ring at frequencies defined as: 100, 250, 500, 600, 750, and 1000 kHz until steady state was achieved. The pressure field was sampled at every voxel at 17 MHz for the last 2 cycles of steady state. A maximum amplitude projection of the pressure field was generated and a 1D intensity profile along Z at the pressure focus was taken for all frequencies. The −3 dB width of this curve was then measured to represent the height of meaningful heating.

Finally, to demonstrate that elevated MHTh temperatures can be maintained throughout the duration of a chemo- or radio- therapeutic session, we ran a 2D k-wave simulation on a simplified breast model in which we initially use 500 kHz CWUS heating at 150 kPa transmit pressure for 120 s, followed by a reduction in pressure to 100 kPa for another 120 s. The model was a 22 cm × 22 cm area with a spatial discretization of ~325 μm based on equation 1. The phantom was a simplified cylindrical breast model in which the background was water, with a 3 cm diameter central circular fibroglandular region, a surrounding 5 cm thick fat region, an outermost 2 mm thick skin layer, with 1 cm diameter tumor region at the fat and fibroglandular interface. Acoustic and thermal properties are listed in Tables 1 and 2 respectively. Separate CWUS delay times were calculated for this phantom using an acoustic forward model as described above. Heating on and off-times followed

the same 1.8 s and 0.2 s on/off scheme. The temperature at the central pixel of the tumor was recorded after each cycle.

Results

Ultrasound thermometry: experimental results

We evaluated the ability of our ring-based UST system to monitor temperature changes in the water flowing through the latex tubes – inclusions - with the lamb tissue phantom and a 20 mm diameter turkey bone. These studies were conducted once on a given tissue sample, to show the feasibility of the current UST ring-array in monitoring temperature change using SS. **Figure 4a** shows the reflection mode output by the system used to localize the tubes and bone. The bone is marked by a blue arrow, the latex tubes with red arrows, and the location of background water for SS comparison is circled in green. **Figure 4b** shows the reconstructed SS values along with the SS standard deviations within both tube locations as well as the background water location at all temperature values. Literature values are also graphed for comparison[42]. The SS values increase with increasing temperature demonstrating agreement with literature, however they are consistently higher than expected values from the literature. We anticipate the observed bias compared to literature is due to the latex tubes being surrounded by higher SS lamb tissue and the limitations of spatial resolution our SS imaging algorithm. With a reconstruction resolution of about 4 mm, volumetric averaging of the pixels near the edge of the tube are artificially increased. Background water shows no considerable SS increase from the room temperature value as this water was not directly heated. **Figure 4c** shows the evolution in the SS images of the phantom at the three temperatures. There is a visually evident increase in the SS at the tube locations compared to the background tissue. The tube locations are shown in blue. We see that the bone shows up as a region of consistently low SS, though we would like to add that the SS reconstruction algorithm was developed with soft-tissue imaging in mind, so any values shown for the bone should be disregarded.

Our final phantom experiment considered the scenario more relevant to breast cancer, using the human abdominal fat phantom. **Figure 5a** shows the reconstructed SS values along with the SS standard deviations within both tube locations at all temperature values. Literature values are also graphed for comparison[42]. Again, the SS values increase in agreement with literature values although they are consistently higher except for inclusion 1 at 40 and 44 ^{o}C. **Figure 5b** shows the evolution in the SS images of the phantom at all six temperatures. There is a visually evident increase in the SS at the tube locations compared to the background tissue. The tube locations are shown in **Figure 5b** where purple is inclusion 1 and red is inclusion 2.

Localized mild hyperthermia induction: in silico results

2D simulations of mild hyperthermia induction using a finite line source and single foci

The results of our 2D simulation for CWUS and subsequent thermal simulation for a single focus at the center of the tumor are seen in **Figure 6**. The indexed numerical breast phantom is seen in **Figure 6a** showing all media types: water, skin, fat, fibroglandular, and tumor. **Figure 6b** shows the initial temperature distribution in which all tissues were set to 37 ^{o}C and water was set to 25 ^{o}C. Following 120 s of heating cycles, the final temperature is shown in **Figure 6c** in both a (i) surface plot and (ii) contour plot where the contours are set at 36, 38, 40, 42, and 44 ^{o}C. **Figure 6d** shows time traces of the average tissue temperature inside tumor, while **Figure 6e** shows the average temperature outside the tumor. The tissue temperature inside the tumor consistently increases as expected since it is nearest to the US focal spot. The tissue outside the tumor begins to decrease in temperature on average because of the cooling water, but once the heated tumor starts to transfer heat to the outside healthy tissue then the average temperature begins to rise as expected. Specific data of note includes: a peak pressure of ~1.49 MPa was reached at the focus, a peak temperature of 48.85 ^{o}C was reached inside the tumor, and 37.1% of the simulated tumor area reached temperatures above 42 ^{o}C after 120 s.

2D simulations of mild hyperthermia induction using a finite line source and multiple foci

The single foci result showed a highly heterogeneous final temperature map of the tumor region. Therefore, it is critical to try and distribute the heat deposition in a more homogeneous fashion. We

therefore used a multiple foci scheme for more homogeneous heat distribution in our simulation. The results of our 2D simulation for CWUS and subsequent thermal simulation for multiple foci about the tumor are seen in **Figure 7**. The same numerical breast phantom from **Figure 6a** is used. Following 210 s of heating cycles, the final temperature is shown in **Figure 7a** in both a (i) surface plot and (ii) contour plot format where the contours are the same as in the previous simulation. **Figure 7b** shows time traces of the average tissue temperature inside tumor and **Figure 7c** shows outside the tumor. The average temperature inside and outside the tumor behaves in a similar way to the previous simulation as expected. However, it is important to note the contour plot also shows a larger area of the medium is above 42 ^{o}C. Specific data of note includes: the peak pressure of each of the 8 foci was between ~1.26 MPa and ~1.45 MPa, a peak temperature of 43.82 ^{o}C was reached inside the tumor, and 83.5% of the simulated tumor area reached temperatures above 42 ^{o}C after 210 s.

3D simulations of mild hyperthermia induction using a finite surface source and single foci

Heat deposition and final temperature maps in a volumetric tissue model were performed using a 3D beamforming scheme to further validate the previous planar simulations. The results of our 3D simulation for CWUS and subsequent thermal simulation for a single focus at the center of the tumor are seen in **Figure 8**. As described in section 3, the full volumetric numerical breast phantom was used for the 3D simulation. Following 120 s of therapy, an XY slice at the middle of the tumor of the final temperature after therapy is shown in **Figure 8a** as both a (i) surface plot and (ii) contour plot where the contours are the same as the previous simulations. **Figure 8b** shows time traces of the average tissue temperature inside the tumor, while **Figure 8c** shows the final temperature outside the tumor. The average temperature inside and outside the tumor behaves in a similar way to the previous single focus simulation as expected. Again, the 3D simulation was run with 100 kPa emitted per point source compared to the previous two 2D simulations (50 kPa). This is due to the increased time it takes to raise the average temperature inside the tumor. Due to the beamforming of the rectangular surfaces of the simulated sensors and the ring geometry, the focused region of

high pressure is similar to a thin cylinder inside the spherical tumor. This is different from the more circular area of high pressure in a circular tumor in the 2D case. Therefore, the 3D simulation has a lower ratio of heated volume to unheated volume when compared to 2D and requires either a longer duration of heating at the same output pressure or a higher output pressure for the same duration. We have chosen the latter; however, the current therapy time is too long for the chosen pressure. Specific data of note includes: the peak pressure was ~1.88 MPa at the focus, a peak temperature of 56.65 ^{o}C was reached inside the tumor, and 96.3% of the simulated tumor area reached temperatures above 42 ^{o}C after 120 s, but this is primarily due to the relatively long therapy time for the maximum pressure at the focus.

In silico studies towards adaptable vertical beamforming

The following demonstrates our investigation into how the vertical beamforming at the focus of our CWUS heating will change based on the transmit frequency. **Figure 9a** shows the steady state pressure field when all 256 elements, which are modeled as 12 mm tall line sources, are firing a 500 kHz CWUS signal focused at the center. **Figure 9b** is an example plot measuring the -3dB width at 500 kHz transmit. **Figure 9c** shows these measurements for all the tested frequencies: 100, 250, 500, 600, 750, and 1000 kHz. The measurements were 108.6, 45.43, 20.15, 16.8, 14.6, 11.4 mm respectively. We hypothesize that it may be possible to optimize the continuous wave frequency to modify the heating height at the target location for different sized tumors. Such optimization and adjustments are possible due to the wideband frequency range of US transducer devices and driving hardware that may provide the possibility of transmitting at a range frequencies. This is critical for appropriate heating of real volumes of pathologic tissue compared to some of the 2D simulations demonstrated here. We look to further investigate this issue in future simulations in order to improve how efficient the system could be at inducing meaningful heating.

In silico studies for MHTh elevated temperature maintenance

Towards the goal of having more advanced treatment plans – once a more customizable system is obtained, we have performed preliminary simulations that show the ability of an all-acoustic MHTh

system to be able to hold the elevated temperature of the pathologic tissue, by reducing the continuous wave pressure amplitude of each element during treatment once the hyperthermic temperature is reached. **Figure 10** demonstrates that this is possible as initially 150 kPa were pumped for heating for the first 120 s, followed by reduction of the transmit pressure to 100 kPa for the remaining 120 s. **Figure 10a** shows the simplified breast phantom that was used for this simulation. **Figure 10b** shows the curve of the central pixel temperature after each heating cycle. This shows that an all-acoustic MHTh system can stabilize pathologic tissue to a hyperthermic temperature throughout the duration of radiation or chemotherapies.

Discussion

We have shown the feasibility of an all-acoustic UST ring-array theranostic system combining both heat induction and temperature monitoring. In the current landscape, advantages of such a system include reduced complexity and increased accessibility when compared to traditional MRI monitoring and microwave systems. We have improved upon previously demonstrated USgFUS systems by being the first group, to our knowledge, to investigate using a single ring-array UST transducer for both heat induction and imaging. Time needed for tomographic imaging has been accounted for in our thermal forward model (necessary for a single transducer system), whereas others have relied on the use of two separate transducers. We demonstrated that SS measurements can be performed in two clinically relevant scenarios (1) a soft tissue sarcoma mimic – using lamb tissue as the base with an embedded bone (**Figure 4**), and (2) a breast cancer mimic – using human abdominal fat (**Figure 5**). The results show that accurate SS measurements can be obtained in presence of a highly reflective and diffractive inclusion such as a bone material (**Figures 4** and **5)**. Additionally, we were able to show *in silico,* that using a similar ring geometry and transducer characteristics as our experimental system, localized heating can be achieved (**Figures 6-8),** even at lower frequencies (500 kHz) and accounting for the time needed to acquire a tomographic scan (100 ms). These results hold promise for future *ex vivo* and *in vivo* studies.

Further, our *in silico* studies looked at the feasibility of taking advantage of the bandwidth of the UST array to vary the central frequency of the continuous wave US beam to change the amount of vertical space that would be heated - **Figure 9**. This offers the advantage of changing the elevational and axial beamforming to adapt to patient-specific needs for a given therapy session. For example, the elevational height could be adjusted from 11 to 108 mm depending on the z-height of the tumor and the bandwidth of the transducer. Lastly, we have shown in **Figure 10** that it is possible to use a UST ring-array for not only inducing heat (≥42 °C) inside an anatomically realistic breast model, but also maintaining that temperature increase while accounting for the time required to perform a tomographic scan for thermometry measurements. Lyon et al.[70] were able to see rapid heat induction within 15 minutes, and sustained heating for ≥30 minutes while maintaining the heated region between 4-8 °C above nominal body temperature [8]. Our results fall in line with what Lyon et al.[70] observed, seeing as **Figure 8** showed our proposed system reaching clinically relevant temperature within approximately 1 minute. Total therapy time will vary based on the treatment being used in conjunction with MHTh. For example, lyso-thermosensitive liposomal doxorubicin (LTLD) requires a circulation time of 30-60 mins over the entire cancerous region[70-72]. Based on the *in silico* results presented in section 4, we believe our proposed all-acoustic MHTh system has the potential to match these benchmarks and will be further evaluated in future *ex vivo* and *in vivo* studies.

We want to address some of the limitations presented in this work. Reviewing the *ex vivo* results, one can observe that we consistently measure higher average SS values of the varying temperature water with relatively wide standard deviation when compared to the values found in the literature - **Figure 4b** and **Figure 5a**. One potential explanation for the large standard deviation could be a combination of volumetric averaging and the limited resolution of the SS measurement algorithm – resolution ~4 mm while the tube diameter is 15 mm. Due to the intrinsic noise levels of our acquisition system, we cannot take advantage of a waveform inversion SS algorithm and have used a ray-based methodology resulting in the worsened resolution. As described in [41,73-75], full-waveform

inversion methods increase the resolution of the reconstructed SS image. Therefore, we reasonably anticipate the resolution of the waveform-driven SS images to reach at least ~2 mm [41,58] - dependent upon the highest frequency used for SS reconstruction, which should greatly diminish the effects of the aforementioned volumetric averaging. However, we do want to mention that the standard deviation is expected even with perfect image reconstruction due to thermal diffusion at the latex tubing boundary resulting in a non-uniform temperature inside the tube. Other complications could result from the limited number of transmitter-receiver pairs for SS inversion, since the ring array is only comprised of 256 elements, as well as artifacts created by the bone for the lamb tissue phantom. One prospective resolution to this would be to acquire a ring array with a greater number of elements as well as a fully programmable platform for modifying the US sequencing (e.g, Verasonics Vantage System, Kirkland, WA). A system like this would provide improved SS calculations and image quality due to the increased number of view angles coupled with implementation of the waveform inversion reconstruction. This would also be the first UST ring-array system for combined MHTh and imaging to the best of our knowledge. Another limitation of our study is the lack of experimental heat induction in *ex vivo* tissue, which is due to the limits of our current UST system described above. As mentioned, we aim to acquire a fully programmable US system for customizable US waveforms (Verasonics). Once such a system is obtained, we are confident that the novel workflow we have proposed in this work will result in successful tissue heating.

Conclusions

This study was motivated by the long-term goal of developing a less complex MHTh all-in-one system that can be combined with radiation and chemotherapies to improve breast cancer treatment outcomes. Here, we have shown experimentally that with an US ring array, changes in SS of water of varying temperatures can be monitored when surrounded by varying materials and in the presence of bone. Our *ex vivo* results demonstrate a clear agreement in SS trend with temperature, taking into consideration the positive shift due to the ray-based inversion

reconstruction resolution limitations coupled with volumetric averaging effects. We have also shown through simulation that deep tissue tumors can reach MHTh level temperatures using an US ring array, elevated tumor temperature can be maintained by adjusting the transducer output pressure, and that modifying the CWUS transmit frequency will change the vertical width of the focal heating region. In future work, we want to improve the uniformity of the final tissue temperature distribution inside the tumor using more complex heating sequences and to obtain the hardware with which we can experimentally demonstrate that US can induce localized heating in an *ex vivo* phantom in the manner proposed.

Acknowledgments

Conflict of Interest Statement

The authors have no conflicts to disclose.

Data Availability

Data will be made available at request.

Reference List

1. Arruebo M, Vilaboa N, Sáez-Gutierrez B, et al. Assessment of the evolution of cancer treatment therapies. *Cancers*. 2011;3(3):3279-3330.

2. Baskar R, Lee KA, Yeo R, Yeoh K-W. Cancer and radiation therapy: current advances and future directions. *International journal of medical sciences*. 2012;9(3):193.

3. Perez-Añorve IX, Gonzalez-De la Rosa CH, Soto-Reyes E, et al. New insights into radioresistance in breast cancer identify a dual function of miR-122 as a tumor suppressor and oncomiR. *Molecular oncology*. 2019;13(5):1249-1267.

4. Jameel J, Rao V, Cawkwell L, Drew P. Radioresistance in carcinoma of the breast. *The Breast*. 2004;13(6):452-460.

5. Chidambaram M, Manavalan R, Kathiresan K. Nanotherapeutics to overcome conventional cancer chemotherapy limitations. *Journal of pharmacy & pharmaceutical sciences*. 2011;14(1):67-77.

6. Stang J, Haynes M, Carson P, Moghaddam M. A preclinical system prototype for focused microwave thermal therapy of the breast. *IEEE Transactions on Biomedical Engineering*. 2012;59(9):2431-2438.

7. Dewey W. Interaction of heat with radiation and chemotherapy. *Cancer Research*. 1984;44(10 Supplement):4714s-4720s.

8. Lyon P. *Targeted release from lyso-thermosensitive liposomal doxorubicin (ThermoDox®) using focused ultrasound in patients with liver tumours*. University of Oxford; 2016.

9. Dunne M, Epp-Ducharme B, Sofias AM, Regenold M, Dubins DN, Allen C. Heat-activated drug delivery increases tumor accumulation of synergistic chemotherapies. *Journal of Controlled Release*. 2019;308:197-208.

10. Song CW, Shakil A, Griffin RJ, Okajima K. Improvement of tumor oxygenation status by mild temperature hyperthermia alone or in combination with carbogen. 1997:626-632.

11. Kampinga H, Dikomey E. Hyperthermic radiosensitization: mode of action and clinical relevance. *International journal of radiation biology*. 2001;77(4):399-408.

12. Stoetzer O, Di Gioia D, Issels RD, et al. Post-Neoadjuvant Gemcitabine and Cisplatin with Regional Hyperthermia for Patients with Triple-Negative Breast Cancer and Non-pCR after Neoadjuvant Chemotherapy: A Single-Institute Experience. *Breast Care*. 2021;16(2):173-180.

13. De-Colle C, Weidner N, Heinrich V, et al. Hyperthermic chest wall re-irradiation in recurrent breast cancer: a prospective observational study. *Strahlentherapie und Onkologie*. 2019;195(4):318-326.

14. Merten R, Ott O, Haderlein M, et al. Long-Term Experience of Chemoradiotherapy Combined with Deep Regional Hyperthermia for Organ Preservation in High-Risk Bladder Cancer (Ta, Tis, T1, T2). *The oncologist*. 2019;24(12):e1341.

15. Wittlinger M, Rödel CM, Weiss C, et al. Quadrimodal treatment of high-risk T1 and T2 bladder cancer: transurethral tumor resection followed by concurrent radiochemotherapy and regional deep hyperthermia. *Radiotherapy and Oncology*. 2009;93(2):358-363.

16. Issels RD, Lindner LH, Verweij J, et al. Effect of neoadjuvant chemotherapy plus regional hyperthermia on long-term outcomes among patients with localized high-risk soft tissue sarcoma: the EORTC 62961-ESHO 95 randomized clinical trial. *JAMA oncology*. 2018;4(4):483-492.

17. Angele MK, Albertsmeier M, Prix NJ, et al. Effectiveness of regional hyperthermia with chemotherapy for high-risk retroperitoneal and abdominal soft-tissue sarcoma after complete surgical resection: a subgroup analysis of a randomized phase-III multicenter study. *Annals of surgery*. 2014;260(5):749.

18. Zwirner K, Bonomo P, Lamprecht U, Zips D, Gani C. External validation of a rectal cancer outcome prediction model with a cohort of patients treated with preoperative radiochemotherapy and deep regional hyperthermia. *International Journal of Hyperthermia*. 2018;34(4):455-460.

19. Schroeder C, Gani C, Lamprecht U, et al. Pathological complete response and sphincter-sparing surgery after neoadjuvant radiochemotherapy with regional hyperthermia for locally advanced rectal cancer compared with radiochemotherapy alone. *International Journal of Hyperthermia*. 2012;28(8):707-714.

20. Tschoep-Lechner KE, Milani V, Berger F, et al. Gemcitabine and cisplatin combined with regional hyperthermia as second-line treatment in patients with gemcitabine-refractory advanced pancreatic cancer. *International journal of hyperthermia*. 2013;29(1):8-16.

21. Maluta S, Schaffer M, Pioli F, et al. Regional hyperthermia combined with chemoradiotherapy in primary or recurrent locally advanced pancreatic cancer. *Strahlentherapie und Onkologie*. 2011;187(10):619.

22. Westermann A, Mella O, Van Der Zee J, et al. Long-term survival data of triple modality treatment of stage IIB–III–IVA cervical cancer with the combination of radiotherapy, chemotherapy and hyperthermia–an update. *International Journal of Hyperthermia*. 2012;28(6):549-553.

23. Heijkoop ST, Franckena M, Thomeer MG, Boere IA, Van Montfort C, Van Doorn HC. Neoadjuvant chemotherapy followed by radiotherapy and concurrent hyperthermia in patients with advanced-stage cervical cancer: a retrospective study. *International Journal of Hyperthermia*. 2012;28(6):554-561.

24. Fotopoulou C, Cho C-H, Kraetschell R, et al. Regional abdominal hyperthermia combined with systemic chemotherapy for the treatment of patients with ovarian cancer relapse: Results of a pilot study. *International Journal of Hyperthermia*. 2010;26(2):118-126.

25. Maluta S, Dall'Oglio S, Romano M, et al. Conformal radiotherapy plus local hyperthermia in patients affected by locally advanced high risk prostate cancer: preliminary results of a prospective phase II study. *International journal of hyperthermia*. 2007;23(5):451-456.

26. Aktas M, de Jong D, Nuyttens JJ, et al. Concomitant radiotherapy and hyperthermia for primary carcinoma of the vagina: a cohort study. *European Journal of Obstetrics & Gynecology and Reproductive Biology*. 2007;133(1):100-104.

27. Wessalowski R, Schneider D, Mils O, et al. An approach for cure: PEI-chemotherapy and regional deep hyperthermia in children and adolescents with unresectable malignant tumors. *Klinische Pädiatrie*. 2003;215(06):303-309.

28. Maluta S, Kolff MW. Role of hyperthermia in breast cancer locoregional recurrence: a review. *Breast care*. 2015;10(6):408-412.

29. Ponce AM, Viglianti BL, Yu D, et al. Magnetic resonance imaging of temperature-sensitive liposome release: drug dose painting and antitumor effects. *Journal of the National Cancer Institute*. 2007;99(1):53-63.

30. Kong G, Anyarambhatla G, Petros WP, et al. Efficacy of liposomes and hyperthermia in a human tumor xenograft model: importance of triggered drug release. *Cancer research*. 2000;60(24):6950-6957.

31. Li L, ten Hagen TL, Hossann M, et al. Mild hyperthermia triggered doxorubicin release from optimized stealth thermosensitive liposomes improves intratumoral drug delivery and efficacy. *Journal of Controlled Release*. 2013;168(2):142-150.

32. Roemer RB. Engineering aspects of hyperthermia therapy. *Annual Review of Biomedical Engineering*. 1999;1(1):347-376.

33. Group ICH, Vernon CC, Hand JW, et al. Radiotherapy with or without hyperthermia in the treatment of superficial localized breast cancer: results from five randomized controlled trials. *International Journal of Radiation Oncology* Biology* Physics*. 1996;35(4):731-744.

34. Odéen H, Parker DL. Magnetic resonance thermometry and its biological applications–Physical principles and practical considerations. *Progress in nuclear magnetic resonance spectroscopy*. 2019;110:34-61.

35. Partanen A, Yarmolenko PS, Viitala A, et al. Mild hyperthermia with magnetic resonance-guided high-intensity focused ultrasound for applications in drug delivery. *International journal of hyperthermia*. 2012;28(4):320-336.

36. Guillemin PC, Gui L, Lorton O, et al. Mild hyperthermia by MR-guided focused ultrasound in an ex vivo model of osteolytic bone tumour: optimization of the spatio-temporal control of the delivered temperature. *Journal of translational medicine*. 2019;17(1):1-19.

37. Zhu L, Partanen A, Talcott MR, et al. Feasibility and safety assessment of magnetic resonance-guided high-intensity focused ultrasound (MRgHIFU)-mediated mild hyperthermia in pelvic targets evaluated using an in vivo porcine model. *International Journal of Hyperthermia*. 2019;36(1):1146-1158.

38. Tillander M, Hokland S, Koskela J, et al. High intensity focused ultrasound induced in vivo large volume hyperthermia under 3D MRI temperature control. *Medical physics*. 2016;43(3):1539-1549.

39. Seip R, Ebbini ES. Noninvasive estimation of tissue temperature response to heating fields using diagnostic ultrasound. *IEEE Transactions on Biomedical Engineering*. 1995;42(8):828-839.

40. Simon C, VanBaren P, Ebbini ES. Two-dimensional temperature estimation using diagnostic ultrasound. *IEEE transactions on ultrasonics, ferroelectrics, and frequency control*. 1998;45(4):1088-1099.

41.   Pratt RG, Huang L, Duric N, Littrup P. Sound-speed and attenuation imaging of breast tissue using waveform tomography of transmission ultrasound data. International Society for Optics and Photonics; 2007:65104S.

42.   Del Grosso V, Mader C. Speed of sound in pure water. *the Journal of the Acoustical Society of America*. 1972;52(5B):1442-1446.

43.   Varghese T, Zagzebski J, Chen Q, et al. Ultrasound monitoring of temperature change during radiofrequency ablation: preliminary in-vivo results. *Ultrasound in medicine & biology*. 2002;28(3):321-329.

44.   Littrup PJ, Duric N, Sak M, et al. Multicenter Study of Whole Breast Stiffness Imaging by Ultrasound Tomography (SoftVue) for Characterization of Breast Tissues and Masses. *Journal of Clinical Medicine*. 2021;10(23):5528.

45.   Sieve R. Ultrasound Imaging. *Radiology Key* blog. 2020. https://radiologykey.com/ultrasound-imaging-3/

46.   Dance D, Christofides S, Maidment A, McLean I, Ng K. Diagnostic radiology physics: A handbook for teachers and students. Endorsed by: American Association of Physicists in Medicine, Asia-Oceania Federation of Organizations for Medical Physics, European Federation of Organisations for Medical Physics. 2014;

47.   Mannaris C, Efthymiou E, Meyre M-E, Averkiou MA. In vitro localized release of thermosensitive liposomes with ultrasound-induced hyperthermia. *Ultrasound in medicine & biology*. 2013;39(11):2011-2020.

48.   Duric N, Littrup P, Roy O, et al. Clinical breast imaging with ultrasound tomography: A description of the SoftVue system. *The Journal of the Acoustical Society of America*. 2014;135(4):2155-2155.

49.   Liu D, Ebbini ES. Real-time 2-D temperature imaging using ultrasound. *IEEE Transactions on Biomedical Engineering*. 2009;57(1):12-16.

50.   Ebbini ES, Ter Haar G. Ultrasound-guided therapeutic focused ultrasound: current status and future directions. *International journal of hyperthermia*. 2015;31(2):77-89.

51.   Vaezy S, Shi X, Martin RW, et al. Real-time visualization of high-intensity focused ultrasound treatment using ultrasound imaging. *Ultrasound in medicine & biology*. 2001;27(1):33-42.

52.   Azhari H. Feasibility study of ultrasonic computed tomography–guided high-intensity focused ultrasound. *Ultrasound in medicine & biology*. 2012;38(4):619-625.

53.   Duric N, Littrup P, Poulo L, et al. Detection of breast cancer with ultrasound tomography: First results with the Computed Ultrasound Risk Evaluation (CURE) prototype. *Medical physics*. 2007;34(2):773-785.

54.   Pattyn A, Kratkiewicz K, Alijabbari N, Mehrmohammadi M, Duric N, Carson PL. Mild-Hyperthermia Generation and Control with a Ring-based Ultrasound Tomography. IEEE; 2021:1-4.

55.   Malik B, Terry R, Wiskin J, Lenox M. Quantitative transmission ultrasound tomography: Imaging and performance characteristics. *Medical physics*. 2018;45(7):3063-3075.

56.   Gemmeke H, Hopp T, Zapf M, Kaiser C, Ruiter NV. 3D ultrasound computer tomography: Hardware setup, reconstruction methods and first clinical results. *Nuclear Instruments and Methods in Physics Research Section A: Accelerators, Spectrometers, Detectors and Associated Equipment*. 2017;873:59-65.

57.   Brenders A, Pratt R. Full waveform tomography for lithospheric imaging: results from a blind test in a realistic crustal model. *Geophysical Journal International*. 2007;168(1):133-151.

58.   Sandhu G, Li C, Roy O, Schmidt S, Duric N. Frequency domain ultrasound waveform tomography: breast imaging using a ring transducer. *Physics in Medicine & Biology*. 2015;60(14):5381.

59.   Li C, Duric N, Huang L. Clinical breast imaging using sound-speed reconstructions of ultrasound tomography data. SPIE; 2008:78-86.

60.   Paige CC, Saunders MA. LSQR: An algorithm for sparse linear equations and sparse least squares. *ACM Transactions on Mathematical Software (TOMS)*. 1982;8(1):43-71.

61.   Klimeš L. Grid travel-time tracing: Second-order method for the first arrivals in smooth media. *pure and applied geophysics*. 1996;148(3):539-563.

62.   Abràmoff MD, Magalhães PJ, Ram SJ. Image processing with ImageJ. *Biophotonics international*. 2004;11(7):36-42.

63. Treeby BE, Cox BT. k-Wave: MATLAB toolbox for the simulation and reconstruction of photoacoustic wave fields. *Journal of biomedical optics*. 2010;15(2):021314.

64. Lou Y, Zhou W, Matthews TP, Appleton CM, Anastasio MA. Generation of anatomically realistic numerical phantoms for photoacoustic and ultrasonic breast imaging. *Journal of biomedical optics*. 2017;22(4):041015.

65. Hasgall PA, Di Gennaro F, Baumgartner C, et al. IT'IS Database for thermal and electromagnetic parameters of biological tissues. doi:10.13099/VIP21000-04-0 itis.swiss/database

66. Absalan H, SalmanOgli A, Rostami R, Maghoul A. Simulation and investigation of quantum dot effects as internal heat-generator source in breast tumor site. *Journal of Thermal Biology*. 2012;37(7):490-495.

67. Duck F. Physical Properties of Tissue: A Comprehensive Reference Book (San Diego, CA: Academic). 1990;

68. Nam K, Zagzebski JA, Hall TJ. Quantitative assessment of in vivo breast masses using ultrasound attenuation and backscatter. *Ultrasonic imaging*. 2013;35(2):146-161.

69. González FJ. Thermal simulation of breast tumors. *Revista mexicana de física*. 2007;53(4):323-326.

70. Lyon PC, Mannaris C, Gray M, et al. Large-volume hyperthermia for safe and cost-effective targeted drug delivery using a clinical ultrasound-guided focused ultrasound device. *Ultrasound in Medicine & Biology*. 2021;47(4):982-997.

71. Poon RT, Borys N. Lyso-thermosensitive liposomal doxorubicin: a novel approach to enhance efficacy of thermal ablation of liver cancer. *Expert opinion on pharmacotherapy*. 2009;10(2):333-343.

72. Wood BJ, Poon RT, Locklin JK, et al. Phase I study of heat-deployed liposomal doxorubicin during radiofrequency ablation for hepatic malignancies. *Journal of Vascular and Interventional Radiology*. 2012;23(2):248-255. e7.

73. Agudo OC, Guasch L, Huthwaite P, Warner M. 3D imaging of the breast using full-waveform inversion. 2018:99-110.

74. Wang K, Matthews T, Anis F, Li C, Duric N, Anastasio MA. Waveform inversion with source encoding for breast sound speed reconstruction in ultrasound computed tomography. *IEEE transactions on ultrasonics, ferroelectrics, and frequency control*. 2015;62(3):475-493.

75. Roy O, Jovanović I, Hormati A, Parhizkar R, Vetterli M. Sound speed estimation using wave-based ultrasound tomography: theory and GPU implementation. International Society for Optics and Photonics; 2010:76290J.
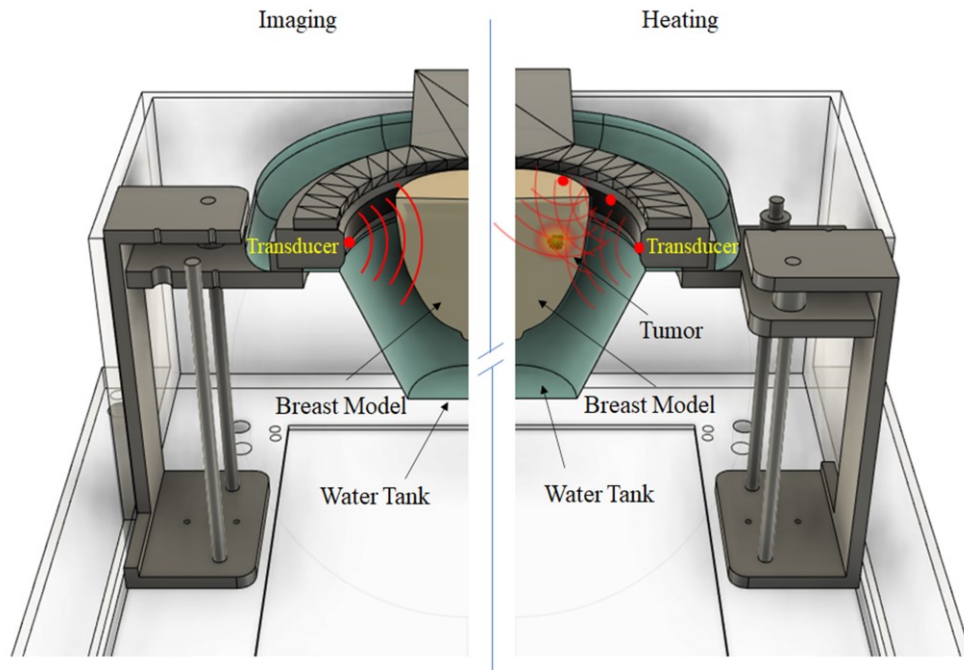
Fig. 1. Schematic of the proposed ring-based UST-guided MHTh theranostic system. For visualization, on the left UST sound speed imaging through sequential element transmission and reception is depicted, and the right half shows the proposed targeted heating using continuous wave acoustic emission from the full ring. The system will operate in time sequenced hyperthermia/imaging regimen.
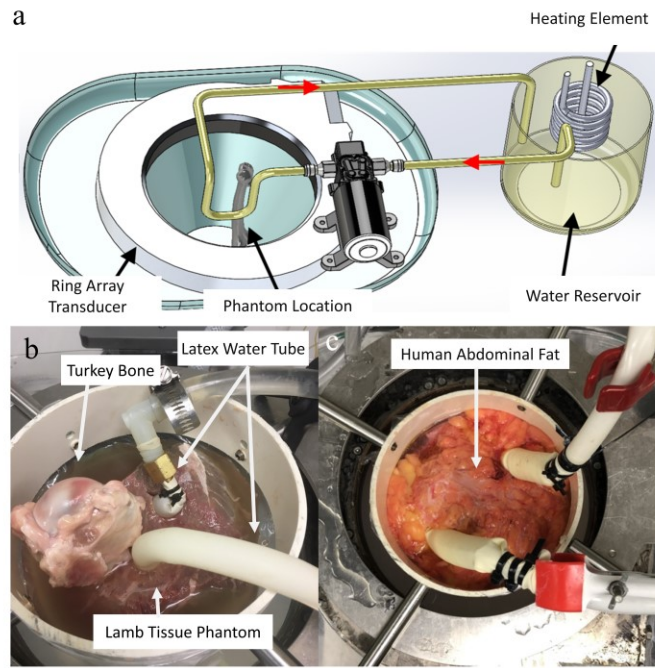
Fig. 2. Experimental design and imaged phantoms. (a) Schematic of system showing location of the transducer, phantom, and method for heating water. (b) Phantom (1) that is made of lamb tissue with an embedded bone with two latex tubes containing flowing temperature-controlled water. (c) Phantom (2) that is made of human abdominal fat with two latex tubes containing flowing temperature-controlled water.
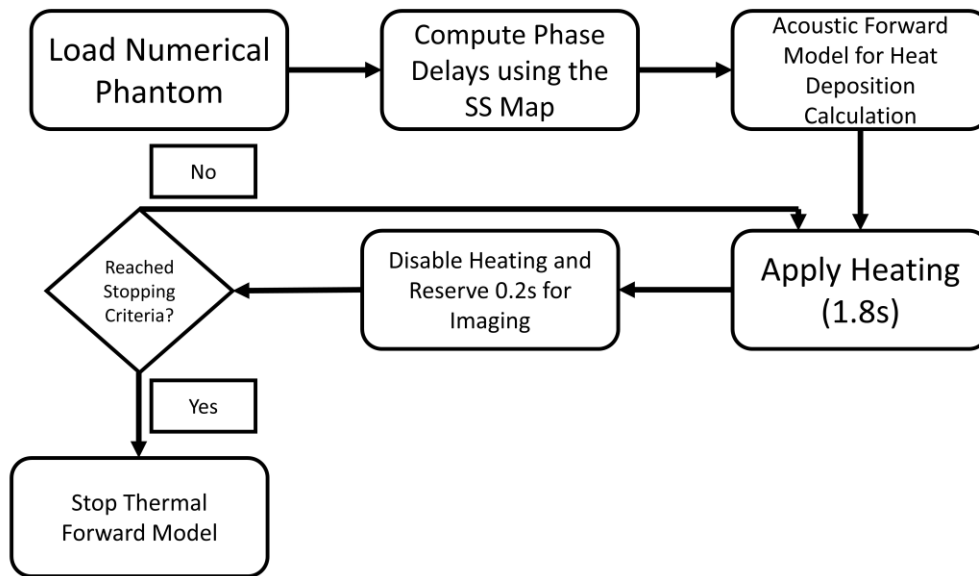
Fig. 3. In silico thermal forward model flow chart. Once the numerical phantom is loaded, the proper phase delays are computed based on the sound speed (SS) - known a priori - of the phantom. Afterwards the heterogeneous SS-corrected phase delayed continuous ultrasound waveforms are used to induce heating. During the thermal simulation, these heating waveforms are only applied for 1.8 s, while 0.2 s are reserved for the imaging sequence that would occur experimentally. Once the stopping criteria are met (defined as a fixed time) the thermal model is stopped.
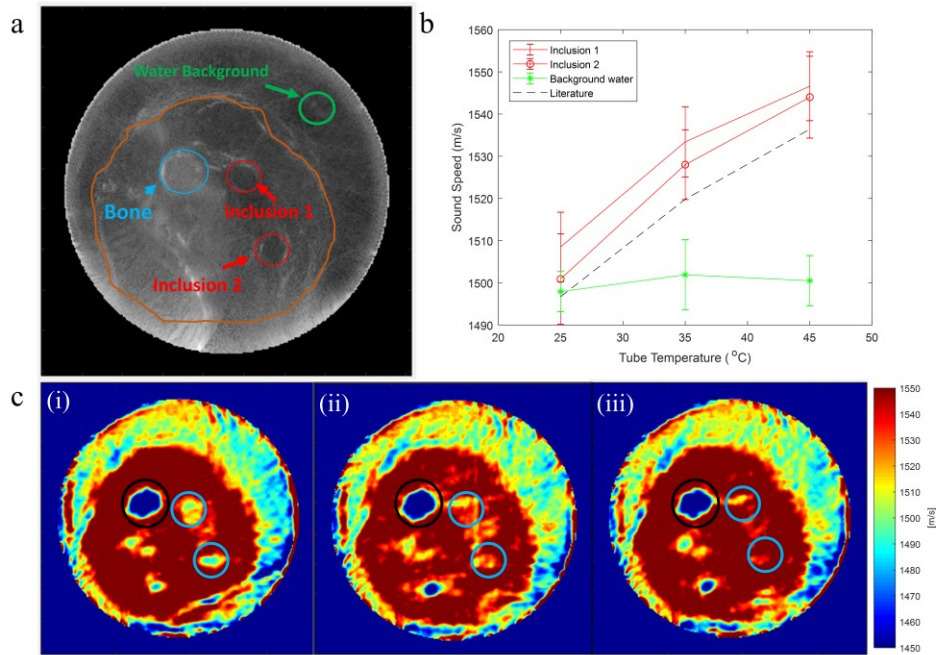
Fig. 4. SS measurement results for the lamb tissue background phantom. (a) Reflection mode image obtained and used for tube/inclusion and bone localization. Blue arrow denotes bone, red arrows denote water tube inclusions, green arrow denotes background water ROI, and the orange outline denotes the boundary of the lamb tissue. (b) Average sound speed and standard deviations at the tube locations and background location at all temperatures compared to literature. (c) SS images at all temperatures (i) 25 ^{o}C, (ii) 35 ^{o}C, (iii) 45 ^{o}C. Blue circles denote inclusion tube locations where the temperature was adjusted. Black circles denote bone location.
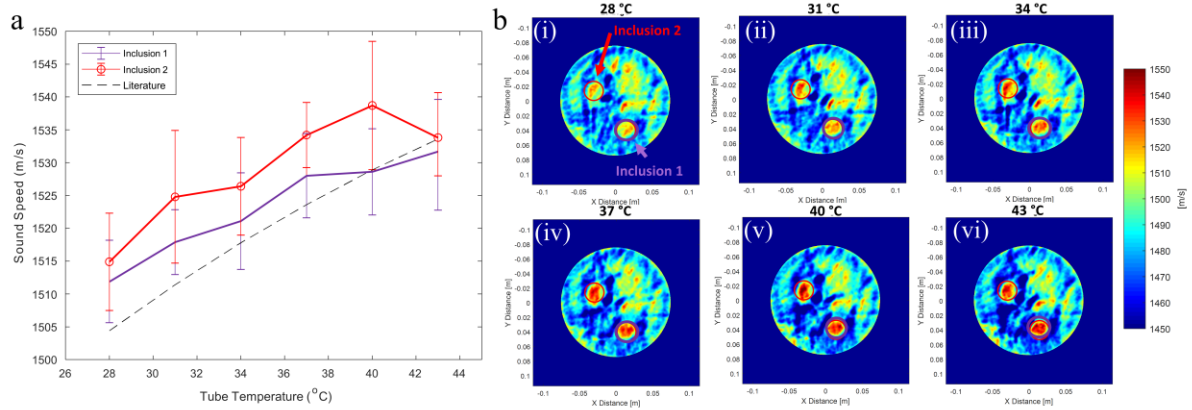
Fig. 5. SS measurement results for the human abdominal fat background phantom. (a) Average sound speed and standard deviations at the tube/inclusion locations. (b) SS images at all temperatures (i) 28 ^{o}C, (ii) 31 ^{o}C, (iii) 34 ^{o}C, (iv) 37 ^{o}C, (v) 40 ^{o}C, (vi) 43 ^{o}C. Where inclusion 1 is purple and inclusion 2 is red.
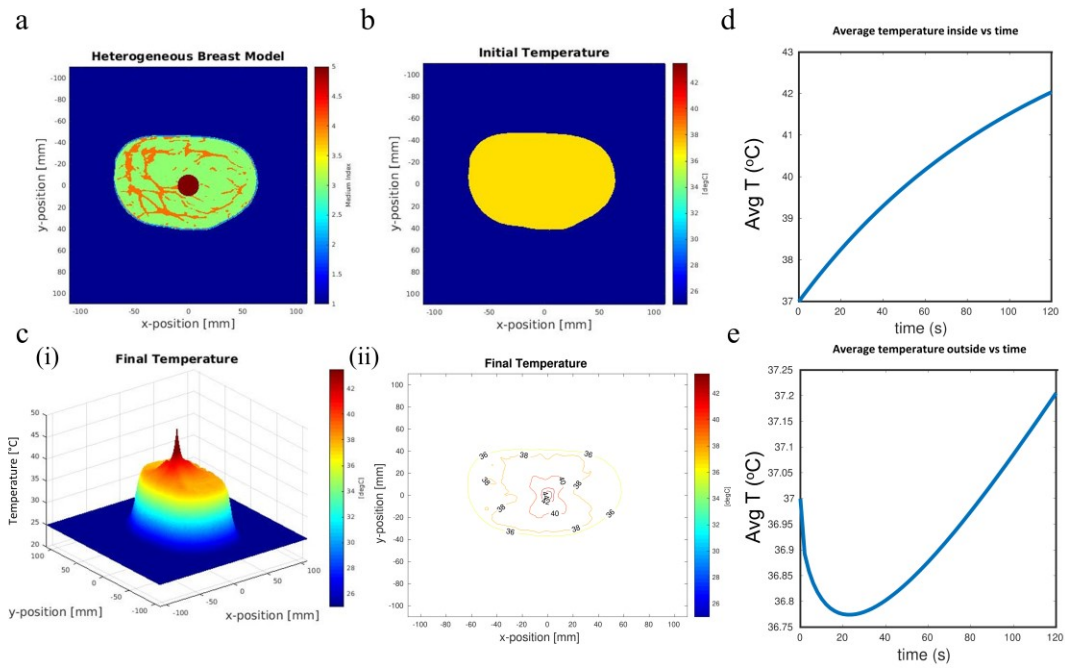
 Fig. 6. 2D in silico MHTh induction results for a single focus. (a) Indexed numerical breast phantom where the media are (1) water, (2) skin, (3) fat, (4) fibroglandular, (5) tumor. (b) Initial temperature map. (c) Final temperature map (i) surface plot and (ii) contour plot where regions with temperature rise to 36, 38, 40, 42, and 44 oC are identified. Time traces of (d) average tissue temperature inside tumor and (e) average tissue temperature outside tumor.
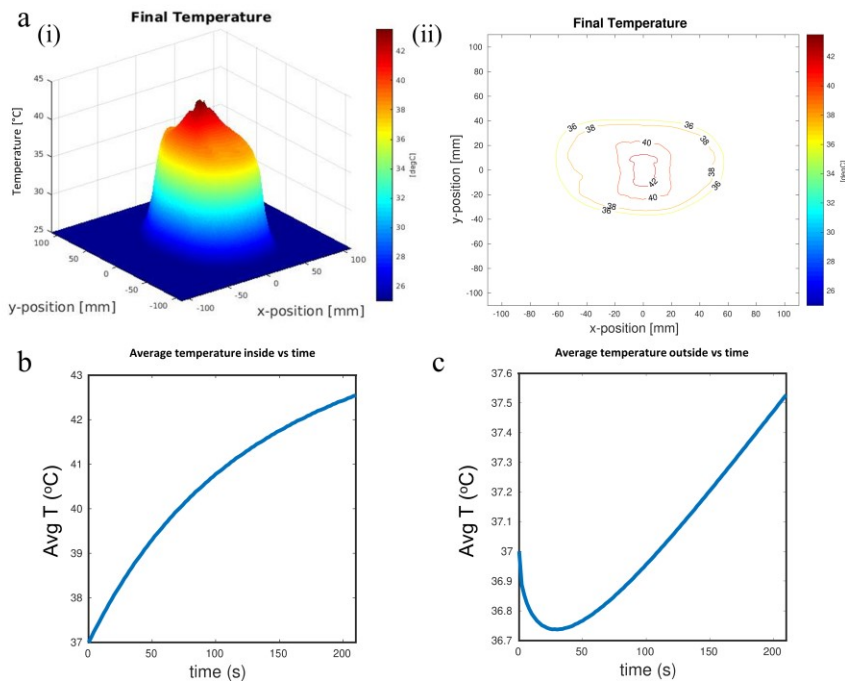
Fig. 7. 2D in silico MHTh induction results for multi-focus. (a) Final temperature map (i) surface plot and (ii) contour plot where contours are at 36, 38, 40, 42, and 44 ^{o}C. Time traces of (b) average tissue temperature inside tumor and (c) average tissue temperature outside tumor.
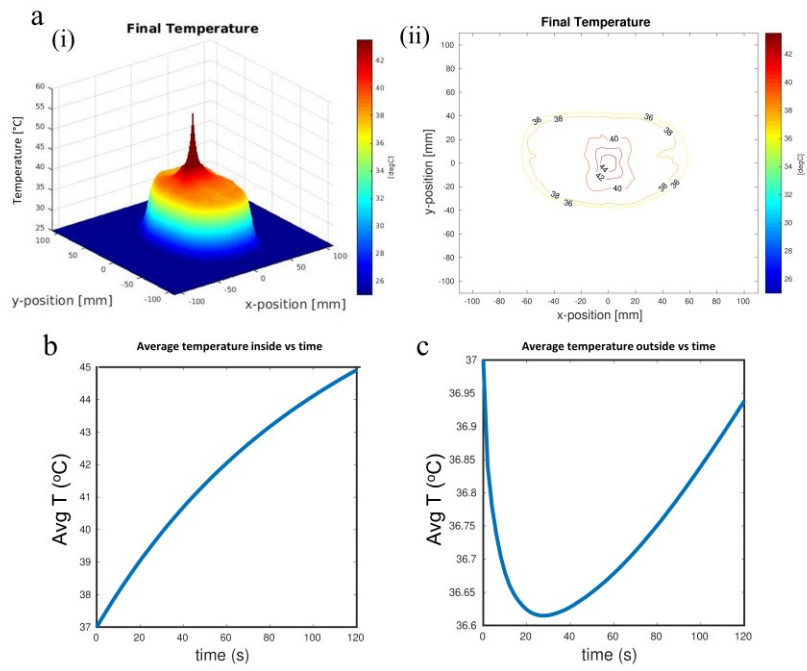
Fig. 8. 3D continuous wave breast MHTh results for a single focus. (a) (i) Isometric views of the indexed numerical breast phantom where the media are (1) water, (2) skin, (3) fat, (4) fibroglandular, (5) tumor. (b) Initial temperature map. (ii) Final temperature map surface plot and contour plot where contours are at 36, 38, 40, 42, and 44 ^{o}C. Time traces of (b) average tissue temperature inside tumor and (c) average tissue temperature outside tumor.
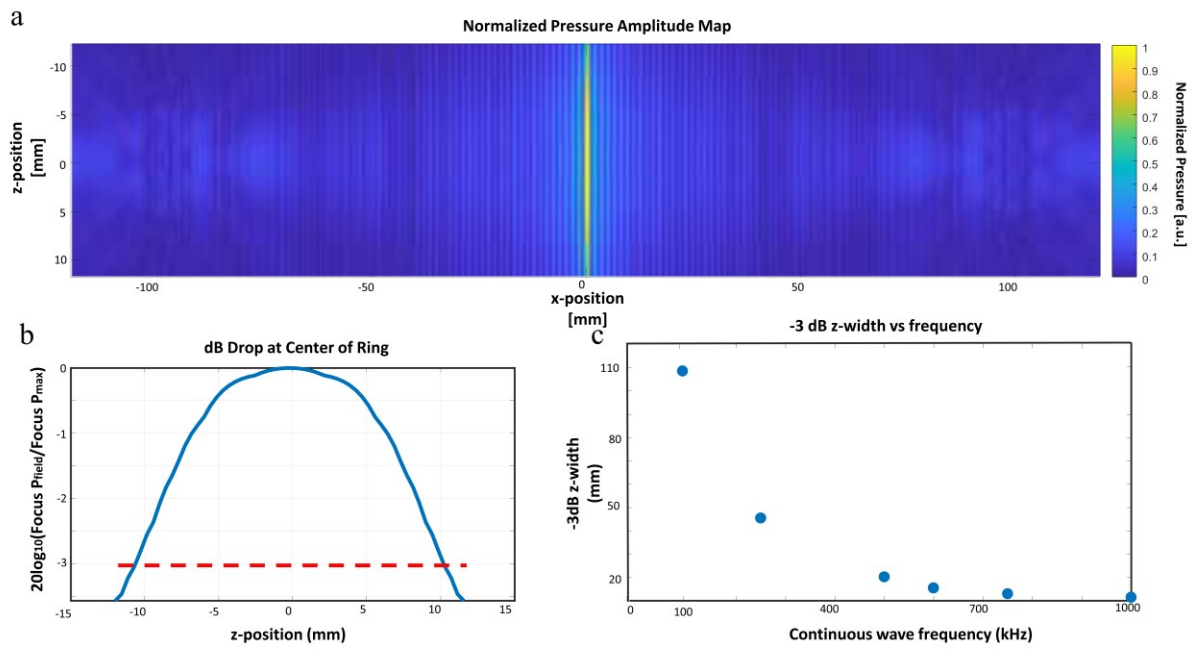
Fig. 9. Analysis of changes in elevational beam width at the focal spot at varying CWUS frequencies. (a) XZ slice of pressure field for 500 kHz frequency output, (b) measurement of -3 dB Z width for 500 kHz field, and (c) plot of –3 dB width for various frequencies: 100, 250, 500, 600, 750, 1000 kHz.
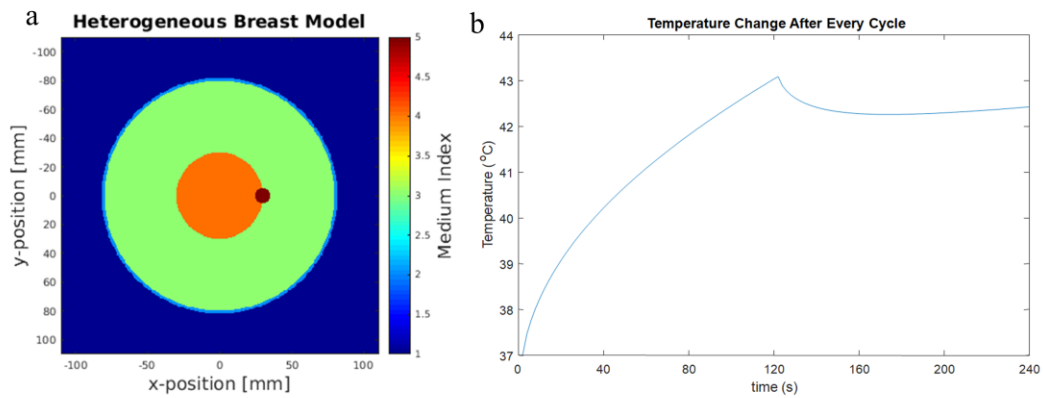
Fig. 10. UST-guided hyperthermia system validation of elevated temperature maintenance. (a) Indexed numerical breast phantom where the media are (1) water, (2) skin, (3) fat, (4) fibroglandular, (5) tumor. (b) Temperature change versus time plot demonstrating the ability of an all ultrasound-based MHTh system to be able to maintain hyperthermic temperatures in pathologic tissue. 120 s of 150 kPa were emitted by all elements to elevate the temperature to 43 ^{o}C followed by a decreased emission by each element of 100 kPa for an additional 120 s to maintain the temperature at around 42 ^{o}C.

TABLE 1. Tissue properties for ultrasound model.

	Water	Skin	Fat	Fibroglandular	Tumor
Density (kg/m^3)	994	1109	911	1041	1050
SS (m/s)	1482	1624	1440	1505	1573
Attenuation (dB/MHz/cm)	0.0022	3	0.5	0.5	1.02

TABLE 2. Tissue properties for thermal diffusion model.

	Water	Skin	Fat	Fibroglandular	Tumor
Thermal conductivity (W/m/K)	0.6	0.37	0.21	0.33	0.564
Specific heat (J/kg/K)	4178	3391	2348	2960	3770
Perfusion (1/s)	0	0.00222	0.000425	0.000425	0.009